Plasma Physics and Controlled Fusion

Gyro-kinetic simulation of trapped electron collision effects on low-frequency drift-wave instabilities in tokamak plasmas

To cite this article before publication: Yuqiang Tao *et al* 2024 *Plasma Phys. Control. Fusion* in press https://doi.org/10.1088/1361-6587/ad42d3

Gyro-kinetic simulation of trapped electron collision effects on low-frequency drift-wave instabilities in tokamak plasmas

Tao. Y.Q.[1*], Wang L.[2], Xu G.S.[2], Chen R.[2], Yan N.[2], Sun P.J.[2], Yang Q.Q.[2], Lin X.[2], Ye Y.[3]

[1]School of Physics and Electronic Information, Anhui Normal University, Wuhu 241000, China

[2]Institute of Plasma Physics, Chinese Academy of Sciences, Hefei 230031, China

[3]Institute of Energy, Hefei Comprehensive National Science Center, Anhui, Hefei, 230031, China

E-mail: yuqiang.tao@ahnu.edu.cn

December, 2023

Abstract

Low-frequency drift-wave instabilities play an important role in the radial transport of present tokamaks, and trapped electron collisions can significantly influence the instabilities. In this paper, the effects of trapped electron collisions on these instabilities are investigated based on linear gyro-kinetic simulation. The basic numerical techniques including dispersion relation integral method and orthogonal basis function expansion are presented in detail with necessary benchmark work. The results show that in medium gradients, the increase of trapped electron proportion promotes the growth rate and radial heat transport largely for quasi-linear TEMs and ITG modes, and trapped electron collisions have strong stabilizing effects, especially for the TEMs driven by electron temperature gradient. Two distinctive branches, named as Mode #1 and #2, are investigated in steep gradients. Both behave varied instability nature during different range of normalized wave vector $\hat{k}_\theta$. Mode #1 mainly induces radial heat transport during $\hat{k}_\theta < 0.5$, and is significantly suppressed by the collisions. Mode #2 mainly induces the radial heat transport during $0.4<\hat{k}_\theta < 0.8$, and is largely enhanced by the collisions. When the collisionality is large enough, Mode #2 has stronger transport capacity than the other. Mode #2 at medium wave vector, known as DTEM, may be the mechanism of the ECM observed in EAST H-mode plasmas, in which the collisionality plays an important role in the mode excitation.

Kerwords:

collision, trapped electron, ITG, TEM, tokamak, plasma

1. Introduction

As one of the most attractive alternatives to carbon-dependent energy sources, nuclear fusion may be utilized peacefully through the tokamak, i.e., a magnetic confinement fusion device. It is significant for future advanced tokamaks to maintain the high energy confinement for commercial power generation. Thus, it is necessary to understand and try to control the radial particle and heat transport in tokamak plasmas, which directly influence the energy confinement. In different channels of the radial transport, low-frequency drift-wave instabilities play an important role, including ion temperature gradient (ITG) modes and trapped electron modes (TEMs) [1,2]. And these instabilities are believed to be the main reasons for the low-frequency micro-instabilities observed in tokamak experiments, which is also known as turbulence transport or anomalous transport [3].

Gyro-kinetic theory is widely used to study low-frequency drift-wave instabilities, including the linear theory [4] and nonlinear theory [5]. And global gyro-kinetic codes, such as GTC [6], XGC1 [7] and gKPSP [8–10], achieve great success in studying these instabilities numerically with complex real geometry. However, large computing resources are necessary for these codes, since particle-in-cell (PIC) simulation that they mainly adopt requires tracing massive particles to reduce the intrinsic noise. Some gyro-kinetic codes with remarkable efficiency are also developed to study the linear instabilities in simple one-dimensional ballooning space geometry, including HD7 code [11,12] based on dispersion relation integral or our recent code [13] based on Euler matrix eigenvalue solution. And these efficient codes have already provided significant evidences that impurity seeding for detachment operation can stabilize or destabilize drift-wave instabilities, mainly determined by impurity density gradient scale length [13–18]. In these works, the density fluctuations due to adiabatic and non-adiabatic responses are included in the quasi-neutrality condition, but the impact of trapped electron collisions, also significantly affected by impurities, has not yet been incorporated into the analysis.

Existing experiment and simulation results show that collision effects are important for trapped electrons and have significant influence in drift-wave instabilities. For instance, in EAST H-mode experiments, an edge coherent mode (ECM) is often observed in the steep-gradient pedestal region, and the collisionality plays an essential role in the ECM's excitation and amplitude [19–21]. Simulation results from global gyro-kinetic code GYRO [19] and GTC [22] show that ECM shows the nature of dissipative trapped electron mode (DTEM), arising from collisional de-trapping of the trapped electrons. However, another simulation work from global gyro-kinetic code GEM [23] believes that ECM appears to be collisionless trapped electron mode (CTEM), excited by precessional resonance of the trapped electrons. The results from GEM [23] show that the instability linear growth rate decreases with the collisionality, consistent with the TEM simulation results from the global gyro-kinetic PIC code gKPSP [8], though it seems contradictory with the ECM experimental features [20, 21].

In this paper, we present the one-dimensional gyro-kinetic code based on dispersion relation integral and orthogonal basis function expansion, recently developed for efficiently studying quasi-linear drift-wave instabilities. Based on this code, simulation work is conducted to study trapped electron collision effects in medium gradients, and we find that the collisions have strong stabilizing effects on these instabilities, especially for the TEMs driven by electron temperature gradient. In steep gradients, two distinctive instability branches are investigated, and the collision effects on them are almost opposite. The remainder of this paper is organized as follows. In section 2, the physical model is presented, including basic linear gyro-kinetic theory, dispersion relation integral method and two benchmark cases. In section 3, collision effects on ITG modes and TEMs in medium gradients are investigated separately. In section 4, collision effects in steep gradients are studied with discussion on the validity of ballooning representation and instability nature. Finally, section 5 is devoted to a summary and discussion.

2. Physical model based on dispersion relation integral

2.1. Basic linear gyro-kinetic theory

Low-frequency drift-wave instabilities can be studied by gyro-kinetic theory with the assumptions $\omega/\Omega_{ci} \sim \rho_{ti}/L \sim k_\parallel/k_\perp \ll 1$ [4, 5], where ω and Ω_{ci} are the instability frequency and main ion cyclotron frequency, ρ_{ti} and L are main ion cyclotron radius and typical parameter scale length, and $k_\parallel$ and $k_\perp$ are parallel and perpendicular wave vector respectively.

In this paper, we focus on quasi-linear drift-wave instabilities which exhibit electrostatic nature, and the electromagnetic components are ignored. The main ion cyclotron radius $\rho_{ti} = \upsilon_{ti}/\Omega_{ci}$ with $\upsilon_{ti} = \sqrt{T_i/m_i}$ is used to normalize the wave vector such as $\hat{k}_\theta = k_\theta \rho_{ti}$, and main ion transit frequency υ_{ti}/R is used to normalize the frequency such as $\hat{\omega} = \omega/(\upsilon_{ti}/R)$, where R is the major radius.

The dispersion relation of these instabilities is obtained from the quasi-neutrality condition:

$$\hat{n}_e = \sum_s z_s \hat{n}_s \tag{1}$$

where $\hat{n}_e$ and $\hat{n}_s$ are electron density fluctuation and ion density fluctuation with charge number z_s, normalized by equilibrium electron density n_e.

Ion density fluctuations only include transit components here with adiabatic and non-adiabatic response, and are described by:

$$\hat{n}_s = -f_s \tau_s \hat{\phi} + \int \hat{h}_s J_0(\hat{k}_\perp \hat{\upsilon}_\perp \alpha_s)\, \mathrm{d}^3\hat{\upsilon} \tag{2}$$

where $f_s = z_s n_s/n_e$ is the charge concentration, $\tau_s = T_e/T_s$ is the temperature ratio and J_0 is the Bessel function of zeroth order, originating from the gyro-phase average. Electrostatic potential fluctuation is normalized by $\hat{\phi} = e\tilde{\phi}/T_e$. The coefficient $\alpha_s = \sqrt{(z_i^2 \tau_i m_s)/(z_s^2 \tau_s m_i)}$ originates from the normalized process, which can be seen more clearly in the previous work [13] with the same character form. The non-adiabatic response $\hat{h}_s$ is obtained from the following gyro-kinetic equation.

By utilizing ballooning angle coordinate θ, the directional derivative is simplified as $\vec{b}\cdot\boldsymbol{\nabla} = \frac{1}{qR}\frac{\partial}{\partial\theta}$ where $\vec{b}$ is the unit vector of the magnetic field, q is the safety factor. And the components of wave vector satisfies $\hat{k}_\perp^2 = \hat{k}_\theta^2[1+\hat{s}^2(\theta-\theta_k)^2]$, where $\hat{s} = \mathrm{d}\ln(q)\,/\,\mathrm{d}\ln(r)$ is the magnetic shear and θ_k originates from the coordinate transform with common default value $\theta_k = 0$. By ignoring ion collision terms, the gyro-kinetic equation for ion non-adiabatic response $\hat{h}_s$ is written as [4, 13]:

$$[(\hat{\omega}-\hat{\omega}_{Ds}) + \beta_s \cdot i\frac{\hat{v}_\parallel}{q}\frac{\partial}{\partial\theta}]\hat{h}_s = (\hat{\omega}-\hat{\omega}_{*sT})J_0 F_M f_s \tau_s \hat{\phi} \tag{3}$$

where the coefficient $\beta_s = \sqrt{(\tau_i m_i)/(\tau_s m_s)}$ also originates from the normalized process. $\hat{\omega}_{Ds} = \varepsilon_{ns}\hat{\omega}_{*s} f(\theta)(\hat{v}_\perp^2/2+\hat{v}_\parallel^2)$ is the normalized magnetic drift frequency with $f(\theta) = \cos\theta + \hat{s}(\theta-\theta_k)\sin\theta$, and $\hat{\omega}_{*sT} = \hat{\omega}_{*s}[1+\eta_s(\hat{v}^2/2-3/2)]$ is the normalized pressure gradient drift frequency. $\varepsilon_{ns} = L_{ns}/R$ and $\eta_s = L_{ns}/L_{Ts}$ are typical scale length ratio, with the density gradient scale length $L_{ns} = -(\mathrm{d}\ln(n_s)\,/\,\mathrm{d}r)^{-1}$ and the temperature gradient scale length $L_{Ts} = -(\mathrm{d}\ln(T_s)\,/\,\mathrm{d}r)^{-1}$. $\hat{\omega}_{*s} = \omega_{*s}/(v_{ti}/R)$ is the normalized density gradient drift frequency with $\omega_{*s} = -(ck_\theta T_s)/(z_s e B L_{ns})$. F_M is the particle velocity distribution function, which is set as the standard Maxwell distribution $F_M = \exp(-\hat{v}^2/2)/(2\pi)^{3/2}$ in this paper. The derivation of kinetic equation for comprehensive ion non-adiabatic response can be fully understood by referring to the Ref. [24].

Due to low frequency, the non-adiabatic response of transit electrons is ignored, which is important for electron temperature gradient (ETG) mode, but less important for TEMs and ITG modes. However, the non-adiabatic response of trapped electrons should be retained, since is the main source for TEMs and has significant influence on ITG modes which will be seen later. Thus, electron density fluctuation is written as:

$$\hat{n}_e = \hat{\phi} + \sqrt{2\epsilon}\int \hat{h}_{et}\,\mathrm{d}^3\hat{v} \tag{4}$$

where $\hat{\phi}$ is electron adiabatic response, $\sqrt{2\epsilon}$ is trapped electron ratio with inverse aspect ratio $\epsilon = r/R$, and $\hat{h}_{et}$ is the non-adiabatic response of trapped electrons. Here electron finite gyroradius effect is neglected, thus the value $J_0(k_\perp\rho_{te}) = J_0(0) = 1$ is applied.

The non-adiabatic response of trapped electrons $\hat{h}_{et}$ is also obtained from gyro-kinetic equation with collision term. Normalized process like ion equations is not conducted here, since the time scale of electron motion is much less than that of ion motion. And the gyro-kinetic equation for trapped electrons is written as [25, 26]:

$$[(\omega-\omega_{De}+i\nu_{ei}/\epsilon) + i\frac{v_\parallel}{qR}\frac{\partial}{\partial\theta}]\hat{h}_{et} = -(\omega-\omega_{*eT})F_e\hat{\phi} \tag{5}$$

where Krook collision operator is utilized with the energy-dependent electron-ion collisional deflection frequency ν_{ei}. And $\omega_{De} = \varepsilon_{ne}\omega_{*e}f(\theta)(v_\perp^2/2+v_\parallel^2)$ and $\omega_{*eT} = \omega_{*e}[1+\eta_e(v^2/2-3/2)]$ are electron magnetic drift frequency and pressure gradient drift frequency with $\omega_{*e} = (ck_\theta T_e)/(eBL_{ne})$, similar to ion's definition. F_e is electron velocity distribution function which is also set as the standard Maxwell distribution here.

Though Eq.(3) and Eq.(5) seems similar, the boundary condition varies a lot. The Eq.(3) describes the transit ions with the boundary $\hat{h}_s \to 0$ when $\theta \to \infty$. However, Eq.(5) describes the trapped electrons with banana orbit and is only meaningful when $\theta \in (-\theta_r, \theta_r)$, where θ_r is the turning point in ballooning space and is associated with the pitch angle of electron velocity. It is convenient to introduce a pitch angle variable κ such that $\kappa^2 = [\upsilon^2/2 - \mu B_0(1-\epsilon)]/(2\epsilon\mu B_0)$, where $\mu = \upsilon_\perp^2/2B$ is the magnetic moment. Electrons with $0 \le \kappa \le 1$ are trapped with the turning point $\theta_r = 2\arcsin\kappa$, and electrons with $\kappa > 1$ can transit through the magnetic field [4, 27].

2.2. Dispersion relation integral

The non-adiabatic response is obtained directly by integrating the gyro-kinetic equations, which can be found in [28]. Here we introduce the orthogonal basis function to expand the electrostatic potential as:

$$\hat{\phi}(\theta) = \sum_m \hat{\phi}_m h_m(\theta) \tag{6}$$

$$h_m(\theta) = \sqrt{\frac{1}{\theta_d 2^m m! \sqrt{\pi}}} \exp\left\{-\frac{(\theta/\theta_d)^2}{2}\right\} H_m(\theta/\theta_d) \tag{7}$$

where θ_d is the width of Gauss function, and $H_m(x)$ is the m-th order Hermite polynomial with $H_0(x) = 1, H_1(x) = 2x, H_m(x) = 2xH_{m-1}(x) - 2(m-1)H_{m-2}(x)$. The basis function is orthogonal as $\int_{-\infty}^{\infty} \mathrm{d}x\, h_m(x)h_n(x) = \delta_{mn}$.

The quasi-neutrality condition, i.e., Eq.(1), can be written as:

$$M_{mn}\hat{\phi}_m = 0 \tag{8}$$

$$M_{mn} = (1 + \sum_s z_s f_s \tau_s)\delta_{mn} + M_{mn}^{et} - M_{mn}^{i} \tag{9}$$

where M_{mn}^{et} comes from the non-adiabatic response of the trapped electrons, and M_{mn}^{i} comes from the non-adiabatic response of the transit ions.

The contribution M_{mn}^{i} is easily obtained as:

$$M_{mn}^{i} = \int_{-\infty}^{\infty} h_n(\theta)\,\mathrm{d}\theta \int_{-\infty}^{\infty} h_m(\theta')\,\mathrm{d}\theta' \int_0^{\infty} \mathrm{d}\hat{\upsilon}_\perp \int_0^{\infty} \mathrm{d}\hat{\upsilon}_\parallel \sum_s K_s \tag{10}$$

$$K_s = 2\pi\hat{\upsilon}_\perp \frac{-iq}{\beta_s\hat{\upsilon}_\parallel} F_M z_s f_s \tau_s J_0(\theta)(\hat{\omega} - \hat{\omega}_{*sT}) J_0(\theta') \exp\left(+iI_{\theta'}^{\theta}\right) \tag{11}$$

$$I_{\theta'}^{\theta} = \frac{q}{\beta_s\hat{\upsilon}_\parallel} \cdot \mathrm{sign}(\theta - \theta')\{\hat{\omega}(\theta - \theta') - \varepsilon_{ns}\hat{\omega}_{*s}(\frac{\hat{\upsilon}_\perp^2}{2} + \hat{\upsilon}_\parallel^2) \int_{\theta'}^{\theta} f(\theta'')\,\mathrm{d}\theta''\} \tag{12}$$

Above quadruple integral can be further simplified to triple integral when standard Maxwell distribution is applied, which is used in the gyro-kinetic code HD7 [12, 14].

The contribution M_{mn}^{et} from the non-adiabatic response of the trapped electrons is much complex. A widely used technique is expanding Eq.(5) in ω/ω_{be} [12, 26] with standard Maxwell distribution assumption, where $\omega_{be} = \epsilon^{1/2}\upsilon_{the}/qR$ is the thermal electron bounce frequency, yielding:

$$
\begin{aligned}
M_{mn}^{et} = & -\sqrt{\frac{2\epsilon}{\pi}} \int_{-\infty}^{\infty} h_n(\theta)\, \mathrm{d}\theta \int_0^{\infty} \mathrm{d}t\, \sqrt{t} e^{-t} \\
& \times \int_0^1 \frac{\hat{\omega} - \hat{\omega}_{*eT}}{\hat{\omega} - \hat{\omega}_{De} + i\hat{\nu}_{ei}/(\epsilon t^{3/2})} \frac{\mathrm{d}\kappa^2}{4K(\kappa)} \\
& \times \sum_{j=-\infty}^{j=+\infty} g(\theta - 2j\pi, \kappa) \times \int_{-\infty}^{\infty} \mathrm{d}\theta'\, g(\theta', \kappa) h_m(\theta' - 2j\pi)
\end{aligned} \tag{13}
$$

where $t = v^2/(2T_e/m_e)$ and $g(\theta, \kappa) = \int_{-\theta_r}^{\theta_r} \mathrm{d}\theta'\, \delta(\theta - \theta')/\sqrt{\kappa^2 - \sin^2(\theta'/2)}$. The normalized frequency $\omega_{*eT} = \hat{\omega}_{*e}[1 + \eta_e(t - 3/2)]$ is the same as that in Eq.(5) with $\hat{\omega}_{*e} = \omega_{*e}/(v_{ti}/R) = z_i\tau_i\hat{k}_\theta/\varepsilon_{ne}$, whereas electron magnetic drift frequency has been averaged as $\hat{\omega}_{De} = \hat{\omega}_{*e}\varepsilon_{ne}t\{2E(\kappa)/K(\kappa) - 1 + 4\hat{s}[E(\kappa)/K(\kappa) - (1-\kappa^2)]\}$, where $K(\kappa)$ and $E(\kappa)$ are the full elliptic integrals of the first and second kind. We use a more common variable, the collisionality $\nu_e^* = \nu_{ei}/\epsilon\omega_{be}$ [19, 22], to represent the normalized collision frequency $\hat{\nu}_{ei}\big|_{v=v_{the}} = \nu_e^*\epsilon^{3/2}\sqrt{2m_i\tau_i/m_e}/q$, in which $\sqrt{2}$ arises from the difference of thermal velocity definition, i.e., $v_{ti} = \sqrt{T_i/m_i}$, $v_{the} = \sqrt{2T_e/m_e}$.

In numerical aspect, the frequency at a fixed wave vector is obtained by setting the determinant of the square matrix $[M_{mn}]$ to zero. To promote the efficiency, basic preparation is conducted firstly for the parameters independent on the wave vector and frequency. Then it only consumes $\sim$ 1min to obtain one $(\hat{k}_\theta, \hat{\omega})$ point for quasi-linear TEMs and ITG modes.

The radial heat transport coefficient $\hat{\chi}_i$ induced by drift-wave instabilities can be further obtained based on quasi-linear mixing length estimation [14], in which the averaged eigenfunction width $\langle\theta^2\rangle^{1/2}$ is a crucial parameter, written as:

$$
\langle\theta^2\rangle^{1/2} = \sqrt{\frac{\int \theta^2 \left|\hat{\phi}(\theta)\right|^2 \mathrm{d}\theta}{\int \left|\hat{\phi}(\theta)\right|^2 \mathrm{d}\theta}} \tag{14}
$$

$$
\hat{\chi}_i \equiv \chi_i/(\frac{2v_{ti}}{z_i R}\rho_{ti}^2) = \frac{\hat{\gamma}}{(\hat{k}_\theta\hat{s})^2\langle\theta^2\rangle} \tag{15}
$$

2.3. Benchmark work

The first benchmark case is about the pure ITG modes with $\epsilon = r/R = 0$ in two ion species condition. The following parameters are used as $\hat{s} = 0.8, q = 1.5, R/L_{ne} = 5, \tau_s = T_e/T_s = 1, R/L_{Ts} = 25 (s = i, z)$ in hydrogen plasmas, and the impurity species is fully-ionized carbon with $f_z = 0.1, R/L_{nz} = -30$. As shown in Fig.1, the calculated growth rates and real frequencies are almost the same as that from recently developed matrix eigenvalue method (MAT) [13] in the whole range of wave vectors. And the results are also highly agreed with that from the gyro-kinetic code HD7 [15], except that small discrepancies appear in small or large wave vectors

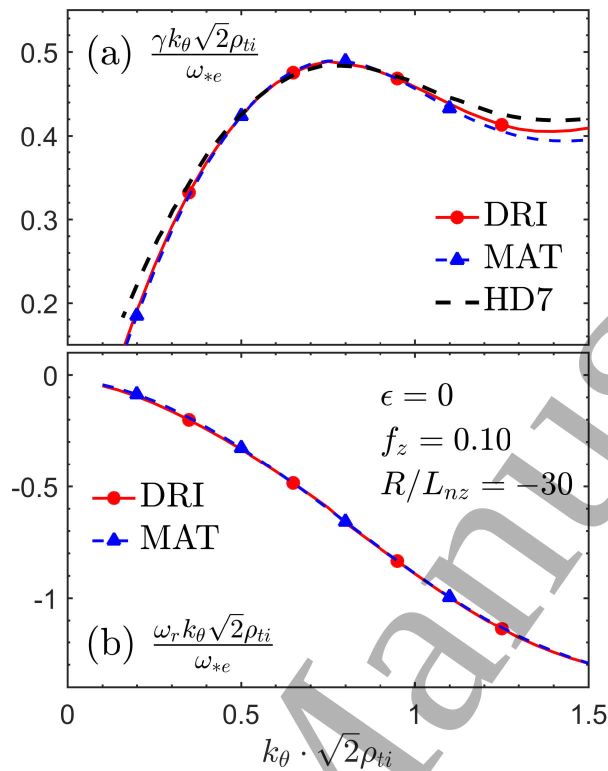

Figure 1: (a) Normalized growth rate $\gamma k_\theta \sqrt{2}\rho_{ti}/\omega_{*e}$ and (b) normalized real frequency $\omega_r k_\theta \sqrt{2}\rho_{ti}/\omega_{*e}$ versus normalized wave vector $k_\theta \sqrt{2}\rho_{ti}$ for pure ITG modes. The data for DRI are from the dispersion relation integral developed in this paper. Other data are from the previous method MAT [13] and gyro-kinetic code HD7 [15].

The second benchmark case is about the coexistence of TEMs and ITG modes by scanning $\eta_i = L_{ni}/L_{Ti}$ in pure hydrogen plasmas, with the parameters $\hat{s} = 1.5, q = 2, \tau_i = 1, \varepsilon_{ne} = L_{ne}/R = 0.2, \eta_e = L_{ne}/L_{Te} = 2, \epsilon = 0.2, k_\theta \rho_{ti} = 0.5/\sqrt{2}, \nu_e^* = 0$ which is abbreviated as case A later. Previous researches [11, 17] show that in medium gradient region, strong ion temperature gradient significantly destabilizes ITG modes, but stabilizes the TEMs. Here constant $L_{ni} = L_{ne}$ is kept, and large η_i means strong ion temperature gradient. As shown in Fig.2, both growth rates and real frequencies for TEMs and ITG modes are well consistent with HD7's results [17], though slight differences appear at large η_i. The TEM growth rate decreases with η_i, whereas the ITG growth rate increases with η_i. There is a proper η_i range for the coexistence of the TEMs and ITG modes. Besides, the TEM real frequencies are positive, indicating that the TEMs propagate along electron diamagnetic direction. And the real frequencies of the ITG modes are negative, indicating that the ITG modes propagate along ion diamagnetic direction.

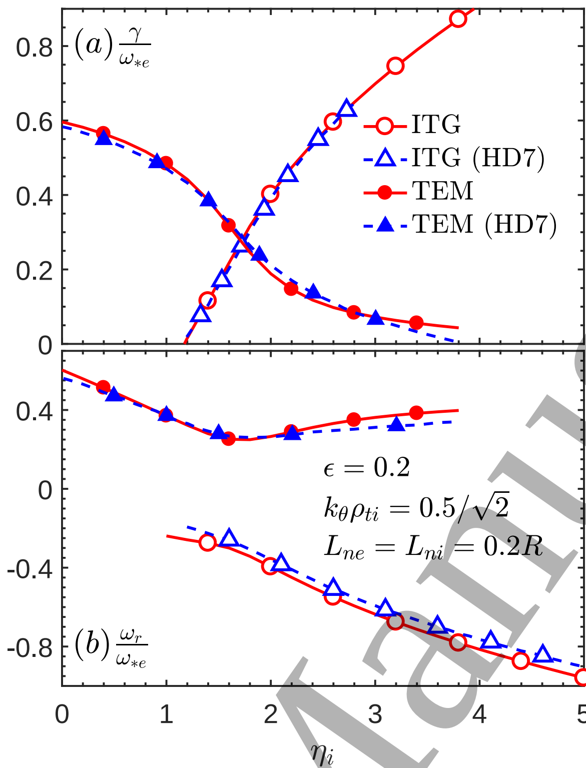

Figure 2: (a) Normalized growth rate γ/ω_{*e} and (b) normalized real frequency ω_r/ω_{*e} versus η_i for TEMs and ITG modes. The HD7's results are from the Ref. [17]

The benchmark works above successfully demonstrate the validity of our newly-developed gyro-kinetic code for quasi-linear TEMs and ITG modes. It is worthy to mention that the slight differences in Fig.1 and 2 may be due to the singularity problem of dispersion relation integral method for transit ion non-adiabatic response when $\hat{v}_\parallel \to 0$ as seen in Eq.(11), which will be further investigated. Besides, there is no necessity to conduct the comparisons when collisions are considered, since the trapped electron collision part $\hat{\nu}_{ei}$ is directly combined with precessional resonance part $\hat{\omega}_{De}$, as shown in Eq.(13).

3. Collision effects in medium gradients

3.1. ITG modes

Further numerical study on the quasi-linear ITG modes with trapped electrons is conducted based on case A with $\varepsilon_{ne} = 0.2, \eta_i = \eta_e = 2$.

Firstly, the influence of the trapped electron proportion ($\sim \sqrt{2\epsilon}$) on quasi-linear ITG modes are studied with $k_\theta \rho_{ti} = 0.6/\sqrt{2}, \nu_e^* = 0$, as shown in Fig.3. Since the inverse aspect ratio ϵ only appears in trapped electron density fluctuations with $\hat{n}_{et} \propto \sqrt{2\epsilon}$, as seen in Eq.(4), it is obvious that the existence of trapped electrons largely enhances the growth rates of the quasi-linear ITG modes, though it only has slight influence on the real frequency and eigenfunction width. Due to $\hat{\chi}_i \propto \hat{\gamma}/\langle\theta^2\rangle$, the existence of trapped electrons also largely enhances the radial heat transport coefficient of the ITG modes. It is worthy to mention that $\hat{\gamma} > 0$ at $\epsilon = 0$ is a signature to distinguish ITG modes, whereas $\hat{\gamma} \to 0$ when $\epsilon \to 0$ for TEMs as seen later, aside from the propagation direction.

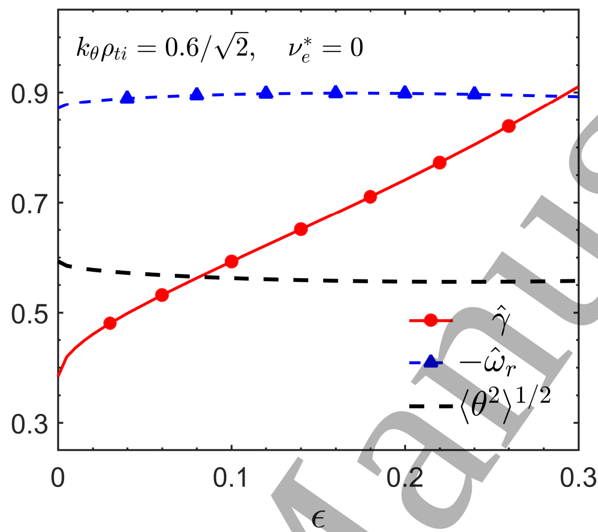

Figure 3: Normalized growth rate $\hat{\gamma}$, negative real frequency $-\omega_r$ and eigenfunction width $\langle\theta^2\rangle^{1/2}$ of the quasi-linear ITG modes versus the inverse aspect ratio ϵ.

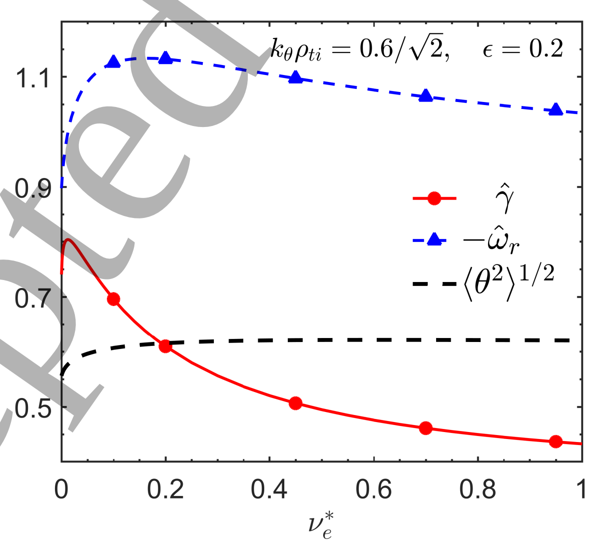

Figure 4: Normalized growth rate $\hat{\gamma}$, negative real frequency $-\omega_r$ and eigenfunction width $\langle\theta^2\rangle^{1/2}$ of the quasi-linear ITG modes versus the collisionality ν_e^*.

Then, we scan the collisionality ν_e^* for quasi-linear ITG modes with $k_\theta \rho_{ti} = 0.6/\sqrt{2}, \epsilon = 0.2$, as shown in Fig.4. The growth rate largely decreases with ν_e^* except at extremely small collionality, indicating that trapped electron collisions help to stabilize the ITG modes. The amplitude of instability real frequency increases with ν_e^* when $\nu_e^* < 0.1$, and is less affected by the collisions when $\nu_e^* > 0.1$. The influence of trapped electron collisions on eigenfunction width is also slight. Therefore, trapped electron collisions help to damp the radial heat transport largely induced by quasi-linear ITG modes.

The spectra of quasi-linear ITG modes are also presented in three cases: $\epsilon = \nu_e^* = 0$, $\epsilon = 0.2, \nu_e^* = 0$ and $\epsilon = 0.2, \nu_e^* = 0.5$, as shown in Fig.5. The growth rates and radial heat transport coefficients for $\epsilon = 0.2, \nu_e^* = 0$ are much larger than that for $\epsilon = \nu_e^* = 0$, indicating that the existence of the trapped electrons can destabilize the quasi-linear ITG modes. However, the growth rates and radial heat transport coefficients for $\epsilon = 0.2, \nu_e^* = 0.5$ are much lower than that for $\epsilon = 0.2, \nu_e^* = 0$, indicating that the trapped electron collisions can stabilize the quasi-linear ITG modes. The peak location of the growth rates are similar for three cases, whereas the peak location of radial heat transport coefficients differs slightly.

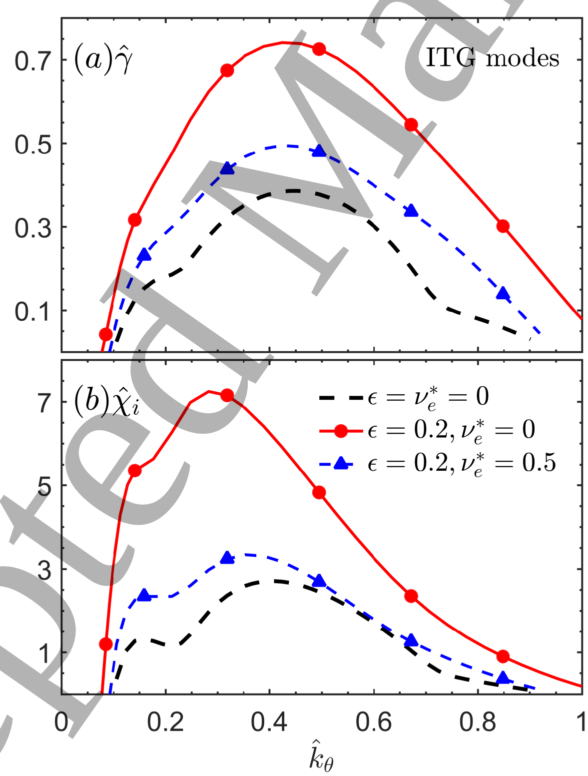

Figure 5: (a) Normalized growth rate $\hat{\gamma}$ and (b) normalized radial heat transport coefficient $\hat{\chi}_i$ versus normalized wave vector $\hat{k}_\theta$ for quasi-linear ITG modes.

3.2. TEMs

To study the effects of trapped electron collisions on TEMs in medium gradients, we set plane ion temperature profile $\eta_i = L_{ne}/L_{Ti} = 0$ based on case A, due to the damping effects of ion temperature gradients on TEMs, as seen in Fig.2(a). Here these TEMs should mainly be classified into CTEM, driven by precessional resonance of trapped electrons.

The driven sources have significant influence on the properties of quasi-linear TEMs. Here three cases are considered: driven source from denisty gradients and temperature gradients with $R/L_{ne} = 10, R/L_{Te} = 10$, driven source mainly from density gradients with $R/L_{ne} = 10, R/L_{Te} = 1$, and driven source mainly from temperature gradients with $R/L_{ne} = 1, R/L_{Te} = 10$.

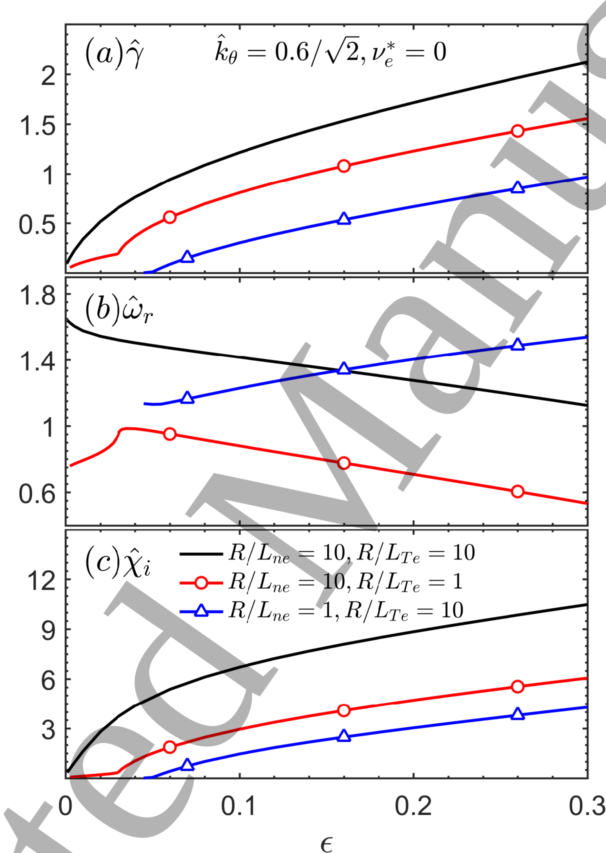

Figure 6: (a) Normalized growth rate $\hat{\gamma}$, (b) normalized real frequency $\hat{\omega}_r$ and (c) normalized radial heat transport coefficient $\hat{\chi}_i$ versus inverse aspect ratio ϵ for quasi-linear TEMs in medium gradients.

As shown in Fig.6, both growth rates and radial heat transport coefficients increase with inverse aspect ratio ϵ, and reaches to zeros when $\epsilon \to 0$ which is much different from quasi-linear ITG modes, as seen in Fig.3. And the relation $\hat{\gamma} \propto \sqrt{\epsilon}$ is almost satisfied, consistent with the analytic results [29]. Real frequencies for $R/L_{ne} = 10, R/L_{Te} = 10$ and $R/L_{ne} = 10, R/L_{Te} = 1$ decrease with ϵ except at small ϵ, whereas real frequencies for temperature driven TEMs ($R/L_{ne} = 1, R/L_{Te}$) increase with ϵ. The driven strength is strongest for $R/L_{ne} = 10, R/L_{ne} = 10$ compared to the others, therefore, it has largest growth rates and radial heat transport coefficients, and has smallest ϵ threshold to excite the instabilities.

The trapped electron collision effects on quasi-linear TEMs also are sensitive to the driven force. As shown in Fig.7(a,c), the temperature gradient driven TEMs ($R/L_{ne}=1, R/L_{Te}=10$) are quickly and completely stabilized by the modest increase of collisionality ν_e^*. However, the density gradient driven TEMs ($R/L_{ne}=10, R/L_{Te}=1$) are slowly stabilized by increased ν_e^* and still remain unstable even at large ν_e^* value. These results are consistent with the results from the gKPSP code with Lorentz collision operator [8]. The trapped electron collisions also tend to reduce the real frequencies of temperature gradient driven TEMs, but promote the real frequencies of density gradient driven TEMs, as shown in Fig.7(b). Combined with ϵ and ν_e^* scanning work, the instabilities for case $R/L_{ne}=10, R/L_{Te}=10$ behave more like density gradient driven type than temperature gradient driven type.

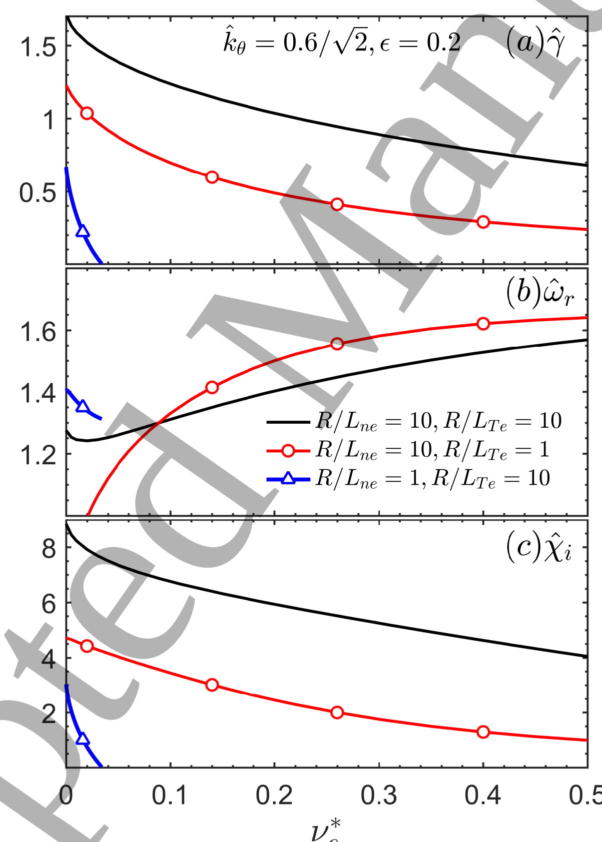

Figure 7: (a) Normalized growth rate $\hat{\gamma}$, (b) normalized real frequency $\hat{\omega}_r$ and (c) normalized radial heat transport coefficient $\hat{\chi}_i$ versus collisionality ν_e^* for quasi-linear TEMs in medium gradients.

Typical spectra for the three cases with or without collisions are also presented in Fig.8. It is clear that trapped electron collisions damp the quasi-linear TEMs in the whole range of wave vectors. On the other hand, the TEM growth rates increase with wave vector, and the outlines are much different from ITG modes, as shown in Fig.5. The radial heat transport induced by TEMs mainly occurs at small wave vector, i.e., long wavelength, whereas the transport induced by ITG modes mainly occurs at medium wave vector, i.e., medium wavelength. Besides, though the growth rates differs a lot for $R/L_{ne} = 10, R/L_{Te} = 1$ and $R/L_{ne} = 1, R/L_{Te} = 10$ without collisions, their radial transport coefficients are similar. And the instabilities for $R/L_{ne} = 10, R/L_{Te} = 10$ have strongest driven force among the three cases, thus, they have largest growth rates and radial heat transport coefficients.

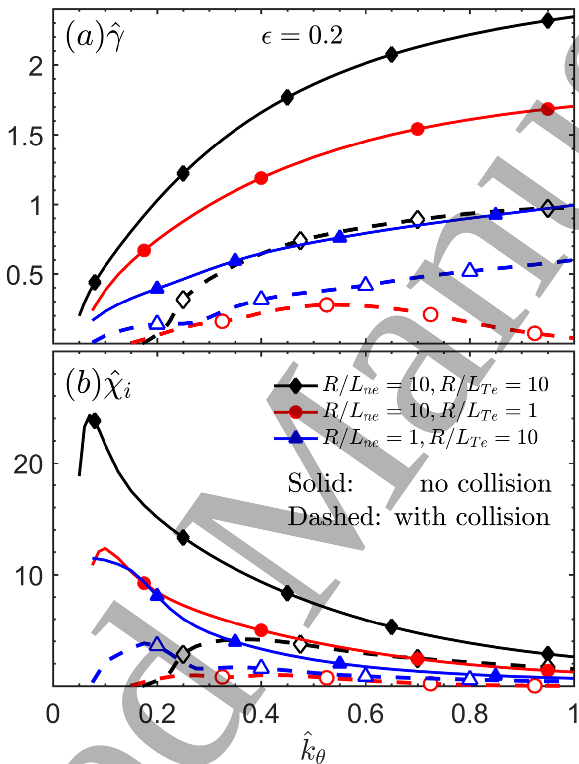

Figure 8: (a) Normalized growth rate $\hat{\gamma}$ and (b) normalized radial heat transport coefficient $\hat{\chi}_i$ versus normalized wave vector $\hat{k}_\theta$ for quasi-linear TEMs in medium gradients. The collisionality $\nu_e^* = 0.5$ is set for the cases with collisions, except for $R/L_{ne} = 1, R/L_{Te} = 10$ with $\nu_e^* = 0.01$.

4. Collision effects in steep gradients

4.1. Validity of ballooning representation

Drift-wave instabilities in steep gradients are much more complex that that in medium gradients. If the plasma gradients are too strong, the ballooning representation may have trouble in describing the mode structure [30, 31]. A dimensionless parameter $\delta = k_\theta \sqrt{2}\rho_{ti}\hat{s}(\sqrt{2}\rho_{ti}/L)^{-1/2}$ is proposed in the Ref. [30] to verify the validity of ballooning representation with $\delta > 1$, where L is the typical gradient scale length and $\sqrt{2}$ originates from the velocity definition difference.

In this section, the typical tokamak edge parameters are utilized as $\hat{s} = 1, q = 2.8, \tau_i =$

$1, L_{ne} = L_{Te} = L_{Ti} = R/69.2$ in pure hydrogen plasmas, which is the same as the Ref. [22] and similar to the Ref. [23]. With major radius $R = 1.6m$, magnetic field $B_t = 2T$ and ion temperature $T_i \sim 500eV$ in typical EAST pedestal, the value δ is around 2 when $k_\theta\sqrt{2}\rho_{ti} = 0.5$.The ballooning representation is still applicable, i.e., $\delta > 1$, during the credible range $\hat{k}_\theta = k_\theta\rho_{ti} > 0.18$ under these parameters. Further argument for the validity of ballooning representation is that the mode behaves mainly like ballooning structure under above parameters from the GTC [22] and GEM [23] simulation.

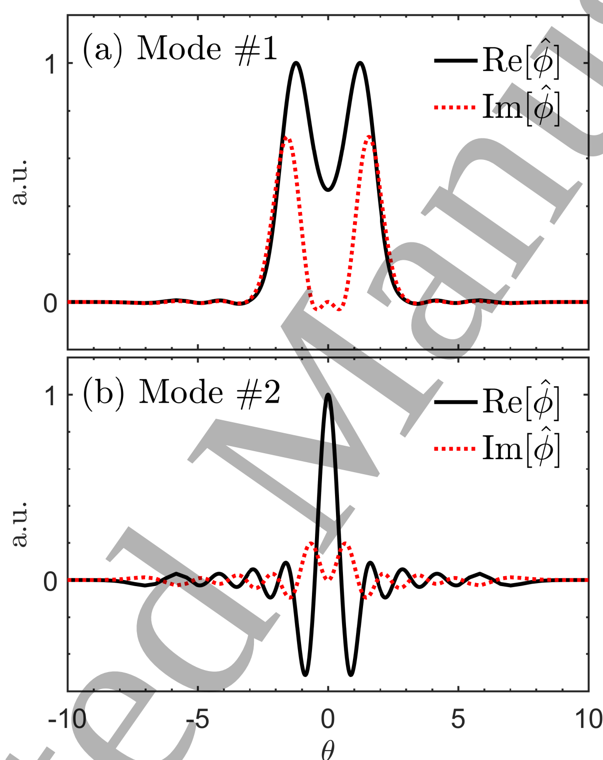

Figure 9: The real part (Re) and imaginary part (Im) of normalized electrostatic potential $\hat{\phi}$ for (a) Mode #1 and (b) Mode #2 versus ballooning angle θ with $\hat{k}_\theta = 0.70, \epsilon = 0.3, \nu_e^* = 2$.

4.2. Instability nature

Two important branches with maximum growth rates are investigated among various kinds of eigenfunctions in steep gradients, marked as Mode #1 and Mode #2. Here, further-simplified zero-dimensional models are also used to help to find the relatively important branches, including Sandberg's model [32] and Cornor's model [27], which have similar results to Mode #1 and Mode #2 respectively. Besides, the two branches also properly correspond to the mode found in the GEM [23] and GTC [22] simulation respectively for the explanation of the ECM oberved in EAST under similar parameters. The typical mode structures are shown in Fig.9 with $\hat{k}_\theta = 0.70, \epsilon = 0.3, \nu_e^* = 2$, and the eigenfunction widths vary a lot. In the rest of this section, the interval of scanning parameters is small enough to obtain smooth growth rate and real frequency curves with continuously changed eigenfunction outlines, aiming to ensure the accuracy of numerical results.

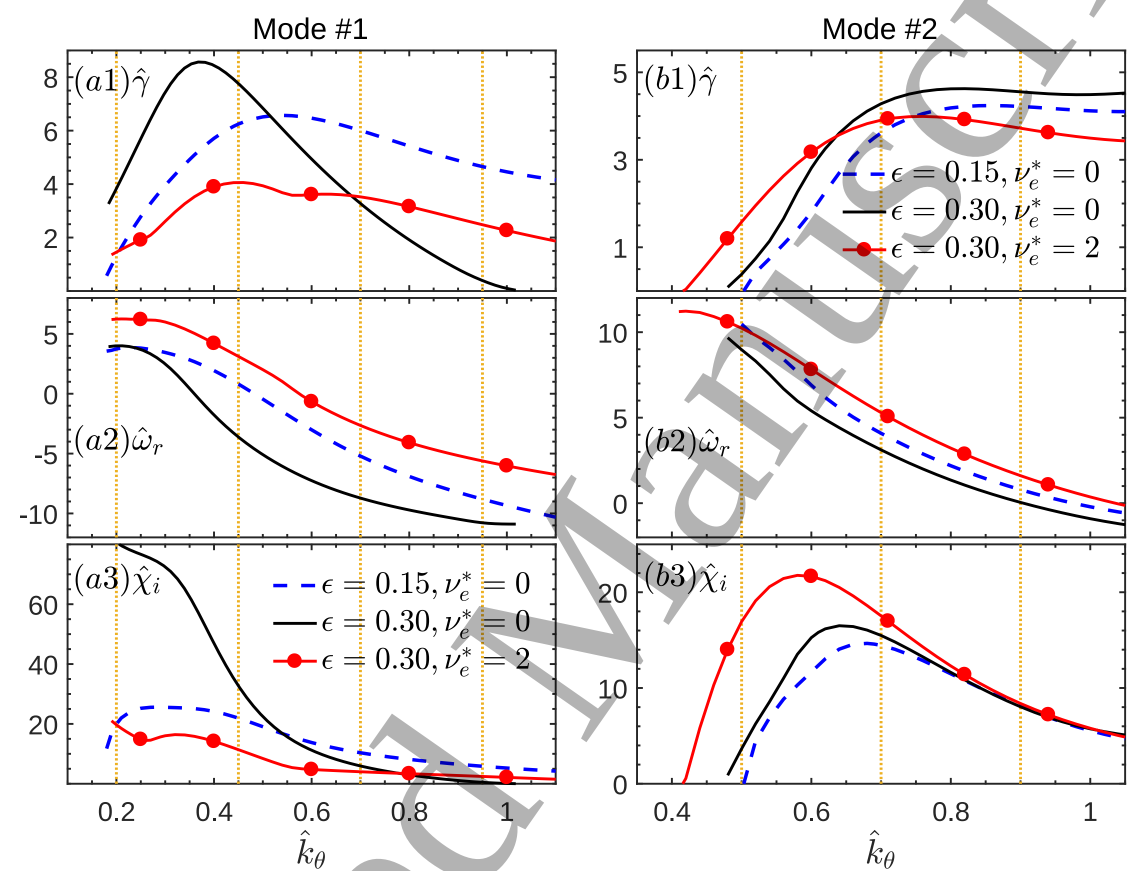

Figure 10: Normalized growth rate $\hat{\gamma}$, real frequency $\hat{\omega}_r$ and radial heat transport coefficient $\hat{\chi}_i$ versus normalized wave vector $\hat{k}_\theta$ with $\epsilon = 0.15, \nu_e^* = 0$ (blue dashed), $\epsilon = 0.30, \nu_e^* = 0$ (black solid) and $\epsilon = 0.30, \nu_e^* = 2$ (red solid with dots). (a1-3) are for Mode #1, and (b1-3) are for Mode #2. The vertical yellow dashed lines represents the $\hat{k}_\theta$ locations for the scanning works later.

As shown in Fig.10, the spectra and radial heat transport coefficients are obtained for Mode #1 and Mode #2 in three cases: $\epsilon = 0.15, \nu_e^* = 0$ (blue dashed); $\epsilon = 0.30, \nu_e^* = 0$ (black solid); $\epsilon = 0.30, \nu_e^* = 2$ (red solid with dots). The proportion of trapped electrons largely influences the spectra of Mode #1, whereas only has modest effects on Mode #2, by comparing the case $\epsilon = 0.15, \nu_e^* = 0$ and $\epsilon = 0.30, \nu_e^* = 0$. For Mode #1, larger ϵ induces larger growth rates $\hat{\gamma}$ and larger radial heat transport coefficients $\hat{\chi}_i$ at small wave vector ($\hat{k}_\theta < 0.5$), but induces smaller $\hat{\gamma}$ and $\hat{\chi}_i$ at large wave vector ($\hat{k}_\theta > 0.5$), which can also be demonstrated by Sandberg's model [32]. The real frequencies of Mode #1 are positive and less affected by ϵ at small wave vector, but they become negative with larger amplitude with increased ϵ at large wave vector. For Mode #2, larger ϵ

induces obvious increase of $\hat{\gamma}$ and $\hat{\chi}_i$ when $0.4 < \hat{k}_\theta < 0.8$, whereas the increase is almost negligible when $\hat{k}_\theta > 0.8$. The real frequencies of Mode #2 decrease with $\hat{k}_\theta$ and are almost positive, which are slightly reduced by larger ϵ. Note that the sigh of real frequencies in steep gradients can not be used to distinguish the instability type, which is much different from that in medium gradients and has also been mentioned in the Ref. [28]. Therefore, unlike conditions in medium gradients, these modes cannot be simply classified into pure TEM or ITG mode in the whole $\hat{k}_\theta$ range, properly due to that each gradient force is strong in steep gradients.

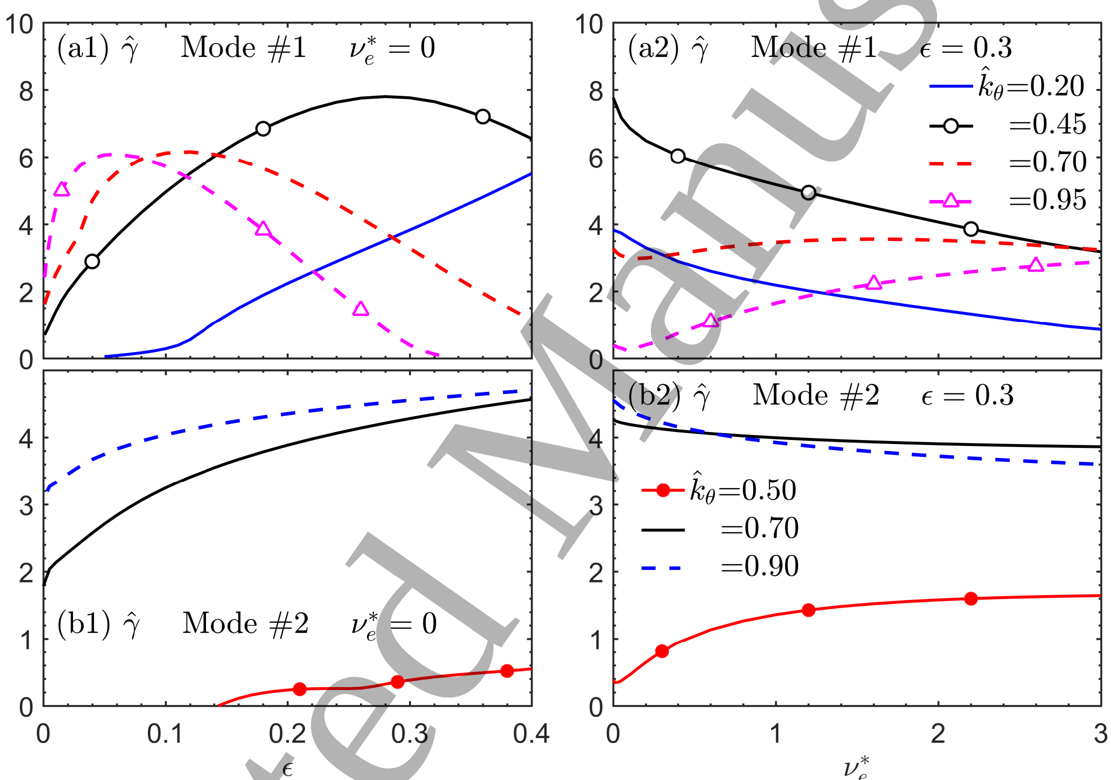

Figure 11: (a1, b1) Scanning inverse aspect ratio ϵ with $\nu_e^* = 0$ and (a2, b2) scanning collisionality ν_e^* with $\epsilon = 0.3$ for Mode #1 at $\hat{k}_\theta = 0.20, 0.45, 0.70, 0.95$ and Mode #2 at $\hat{k}_\theta = 0.50, 0.70, 0.90$.

4.3. Collision effects

Scanning ϵ without collisions at different wave vectors, including $\hat{k}_\theta = 0.20, 0.45, 0.70, 0.95$ for Mode #1 and $\hat{k}_\theta = 0.50, 0.70, 0.90$ for Mode #2, can also reveal the nature difference of two branches. The scanning works start from the point of the lines with $\epsilon = 0.30, \nu_e^* = 0$ in Fig.10, marked with vertical yellow dashed lines. As shown in Fig.11(a1), Mode #1 at small wave vector tends to be pure TEM since $\hat{\gamma}$ increases with ϵ at $\hat{k}_\theta = 0.20$ and reaches to zeros when $\epsilon \to 0$. However, Mode #1 at large wave vector tends to be coupled ITG and TEM, since $\hat{\gamma}$ increases at first and then decreases with increased ϵ, and the ϵ turning point is much smaller at larger wave vector. As shown in Fig.11(b1), Mode #2 at medium wave vector $\hat{k}_\theta = 0.50$ also tends to be pure TEM. However, Mode #2 at large wave vector behaves mainly like ITG mode, since $\hat{\gamma}$ increases with ϵ but is still large when $\epsilon \to 0$.

The difference of these instability nature at varied wave vector can also be shown by studying the collision effects. Scanning the collisionality ν_e^* with $\epsilon = 0.3$ is conducted at different wave vectors, including $\hat{k}_\theta = 0.20, 0.45, 0.70, 0.95$ for Mode #1 and $\hat{k}_\theta = 0.50, 0.70, 0.90$ for Mode #2. The scanning works start from the point of the lines with $\epsilon = 0.30, \nu_e^* = 2$ in Fig.10. For Mode #1, trapped electron collisions have stabilizing effects at small wave vector, but have destabilizing effects at large wave vector, as shown in Fig.11(a2). For Mode #2, trapped electron collisions have strong destabilizing effects at medium wave vector which is consistent with Cornor's model [27], but have weak stabilizing effects at large wave vector, as shown in Fig.11(b2). In fact, at medium wave vector like $\hat{k}_\theta = 0.45$, Mode #2 tends to be mainly driven by collisional de-trapping of the trapped electron, known as DTEM, with strong capacity of radial heat transport, as shown in Fig.10(b3).

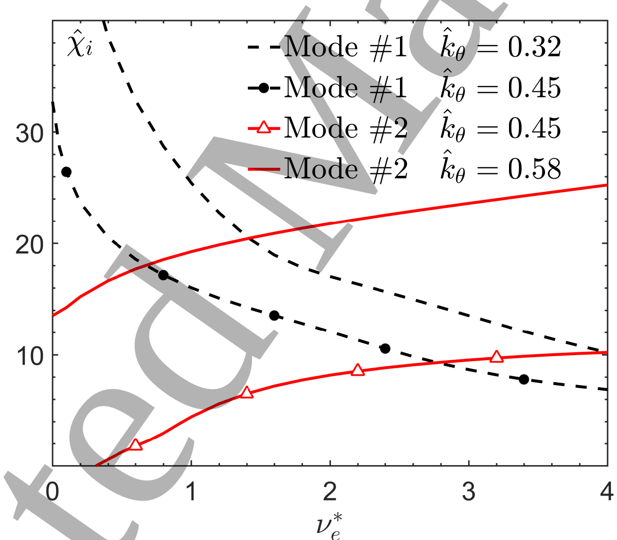

Figure 12: Radial heat transport coefficient $\hat{\chi}_i$ versus the collisionality ν_e^* at $\hat{k}_\theta = 0.32, 0.45$ for Mode #1 and $\hat{k}_\theta = 0.45, 0.58$ for Mode #2 with $\epsilon = 0.3$.

Mode #1 mainly induces radial heat transport at relatively small wave vector ($\hat{k}_\theta < 0.5$), and the transport capacity is severely suppressed by the collisions, as shown in Fig.10(a3) by comparing the case $\epsilon = 0.30, \nu_e^* = 0$ and case $\epsilon = 0.30, \nu_e^* = 2$. On the contrary, Mode #2 mainly induces radial heat transport at medium wave vector ($0.4 < \hat{k}_\theta < 0.8$), and the transport capacity is largely enhanced by the collisions, as shown in Fig.10(b3). To further compare the transport capacity, the radial heat transport coefficient $\hat{\chi}_i$ versus the collisionality ν_e^* with $\epsilon = 0.3$ for Mode #1 and Mode #2 is shown in Fig.12. The scanning works also start from the point of the lines with $\epsilon = 0.30, \nu_e^* = 2$ in Fig.10 at $\hat{k}_\theta = 0.32$ for Mode #1 and $\hat{k}_\theta = 0.58$ for Mode #2, where the radial heat transport mainly occurs. When $\nu_e^* > 1.5$, the heat transport coefficient $\hat{\chi}_i$ induced by Mode #2 at $\hat{k}_\theta = 0.58$ is larger than that induced by Mode #1 at $\hat{k}_\theta = 0.32$. Even at the same wave vector, i.e., $\hat{k}_\theta = 0.45$, as shown in Fig.12, Mode #2 induces larger radial heat transport than the other when $\nu_e^* > 2.8$. Thus, it is convincing that Mode #2 has stronger capacity of radial heat transport than Mode #1 when the collisionality $\hat{\chi}_i$ is large enough.

5. Summary and discussion

In this paper, the basic theory and numerical techniques based on dispersion relation integral and orthogonal basis function expansion are presented in detail, aiming to study the low-frequency drift-wave instabilities efficiently. And a gyro-kinetic code based on one-dimensional ballooning space is developed, and benchmark works have been conducted in two ion species and for the existence of TEMs and ITG modes, which demonstrate the code's validity for studying these instabilities. Though different forms of the collision operator could give varied scaling with the collisonality [27, 33], the Krook collision operator is utilized in this work, which is applicable to study the influencing tendency of trapped electron collisions on the instabilities.

The effects of trapped electron collisions in medium gradients on low-frequency drift-wave instabilities are studied numerically. For quasi-linear ITG modes or TEMs, the increase of trapped electron proportion promotes the growth rates and radial heat transport. However, the collisions have stabilizing effects on these modes. Compared to the TEMs driven by density gradients, the stabilizing effects of trapped electron collisions are much stronger for the TEMs driven by temperature gradients, and only very small collisionality can completely suppress these modes, which is consistent with the gKPSP code's results with Lorentz collision operator [8]. Some experiments on the tokamak such as EAST [34, 35], HL-2A [36], JET [37] and ASDEX-Upgrade [38], show that impurity seeding can suppress the turbulent transport, induce the increase of ion temperature and promote the plasma confinement. And these phenomena may be partly explained by the stabilizing effects from the collisionality, which are usually promoted after impurity seeding. The results may promote the credibility of the compatibility between detachment operation and high confinement for future advanced tokamaks.

Two distinctive branches, named as Mode #1 and #2, are also investigated in steep gradients. Note that the gradient is not too strong, and the ballooning representation is still applicable here. Scanning inverse aspect ratio ϵ and the collisionality ν_e^* are conducted, and both branches behave varied instability nature at different normalized wave vector $\hat{k}_\theta$. Mode #1 at small $\hat{k}_\theta$ behaves as pure TEMs and is strongly stabilized by trapped electron collisions, but it tends to be coupled ITG and TEM at large $\hat{k}_\theta$ and is weakly destabilized by the collisions. Mode #2 tends to be pure TEMs at medium $\hat{k}_\theta$ and is strongly destabilized by trapped electron collisions, but it behaves mainly like ITG modes at large $\hat{k}_\theta$ and is weakly stabilized by the collisions. Mode #1 mainly induces radial heat transport during $\hat{k}_\theta < 0.5$, and is significantly suppressed by the collisions. Mode #2 mainly induces the radial heat transport during $0.4<\hat{k}_\theta < 0.8$, and is largely enhanced by the collisions. When the collisionality is large enough, Mode #2 has stronger capacity of the radial heat transport than Mode #1.

The mode found in GEM code's simulation [23] properly corresponds to Mode #1 at small wave vector, but it may not be the reasons for the ECM observed in EAST H-mode plasmas [19–21] since the collision stabilizing effects contradict the ECM's experimental feature. The mode found in GTC code's simulation [22] properly corresponds to Mode #2 at medium wave vector, known as DTEM, and is properly the mechanism of the ECMs since the dependence on the collisionality and the real frequency are consistent with experimental results. However, only poloidal wave vector k_p of the ECM is measured in experiments at present without the radial component k_r [19–21], whereas the perpendicular wave vector satisfies $k_\perp = \sqrt{k_p^2 + k_r^2}$ [39]. Though the typical tokamak edge parameter used in section 3.4 of this paper and the Ref. [22] are almost consistent with EAST H-mode conditions, the edge safety factor $q_{95} \sim 5$ in EAST [19–21] is usually much higher than the value we set. Besides, limited to measurement resolution, the value of temperature gradient scale length in EAST pedestal has relatively large uncertainty. In the near future, further researches will be conducted by combining the two key factors, i.e., collisionality ν_e^* and impurity density gradient scale length L_{nz}, to obtain comprehensive understanding of the impurity seeding effects, especially in extreme strong gradient regions where the ballooning representation is not applicable any more.

Data availability statement

All data that support the findings of this study are included within the article (and any supplementary files).

Acknowledgments

This work was supported by the National Magnetic Confinement Fusion Energy Program of China under Grant Nos. 2022YFE03020004, 2019YFE03030000, the National Natural Science Foundation of China under Grant Nos. 11975275, 12275312, 12275316, 12305255, the Open Fund of Magnetic Confinement Fusion Laboratory of Anhui Province under Grant No. 2022AMF02001, the Ph.D Research Startup Foundation of Anhui Normal University, and the HFIPS Director's Fund Grant Nos. YZJJ2023QN22.

References

[1] W.M. Tang. Microinstability theory in tokamaks. *Nuclear Fusion*, 18(8):1089, aug 1978.

[2] W. Horton. Drift waves and transport. *Reviews of Morden Physics*, 71(3):735–778, APR 1999.

[3] E.J. Doyle, W.A. Houlberg, Y. Kamada, V. Mukhovatov, T.H. Osborne, A. Polevoi, G. Bateman, J.W. Connor, J.G. Cordey, T. Fujita, X. Garbet, T.S. Hahm, L.D. Horton, A.E. Hubbard, F. Imbeaux, F. Jenko, J.E. Kinsey, Y. Kishimoto, J. Li, T.C. Luce, Y. Martin, M. Ossipenko, V. Parail, A. Peeters, T.L. Rhodes, J.E. Rice, C.M. Roach, V. Rozhansky, F. Ryter, G. Saibene, R. Sartori, A.C.C. Sips, J.A. Snipes, M. Sugihara, E.J. Synakowski, H. Takenaga,

T. Takizuka, K. Thomsen, M.R. Wade, H.R. Wilson, ITPA Transport Physics Topical Group, ITPA Confinement Database, Modelling Topical Group, ITPA Pedestal, and Edge Topical Group. Chapter 2: Plasma confinement and transport. *Nuclear Fusion*, 47(6):S18, jun 2007.

[4] T. M. Antonsen and B. Lane. Kinetic equations for low frequency instabilities in inhomogeneous plasmas. *The Physics of Fluids*, 23(6):1205–1214, 06 1980.

[5] A.J. Brizard and T.S. Hahm. Foundations of nonlinear gyrokinetic theory. *Reviews of Modern Physics*, 79(2):421–468, APR-JUN 2007.

[6] Z. Lin and T.S. Hahm. Turbulence spreading and transport scaling in global gyrokinetic particle simulations. *Physics of Plasmas*, 11(3):1099–1108, 02 2004.

[7] K.H. Kim, J.M. Kwon, C.S. Chang, J.H. Seo, S. Ku, and W. Choe. Full-f XGC1 gyrokinetic study of improved ion energy confinement from impurity stabilization of ITG turbulence. *Physics of Plasmas*, 24(6):062302, 06 2017.

[8] J.M. Kwon, L. Qi, S. Yi, and T.S. Hahm. ITG-TEM turbulence simulation with bounce-averaged kinetic electrons in tokamak geometry. *Computer Physics Communications*, 215:81–90, 2017.

[9] J.H. Seo, H.G. Jhang, and J.M. Kwon. Effects of light impurities on zonal flow activities and turbulent thermal transport. *Physics of Plasmas*, 29(5):052502, 05 2022.

[10] Y.J. Kim, J.M. Kwon, L. Qi, and T.S. Hahm. Extended bounce-kinetic model for trapped electron mode turbulence. *Physics of Plasmas*, 29(4):042103, 04 2022.

[11] J. Q. Dong, S. M. Mahajan, and W. Horton. Coupling of η_i and trapped electron modes in plasmas with negative magnetic shear. *Physics of Plasmas*, 4(3):755–761, 03 1997.

[12] J.Q. Dong. Kinetic micro-instabilities in the presence of impurities in toroidal magnetized plasmas. *Plasma Science and Technology*, 20(9):094005, aug 2018.

[13] Y.Q. Tao and P.J. Sun. Numerical study of impurity effects on ion temperature gradient modes in tokamak edge plasmas based on the Euler matrix eigenvalue method. *Plasma Physics and Controlled Fusion*, 65(8):085001, jun 2023.

[14] J. Li, Z.X. Wang, J.Q. Dong, M.K. Han, Y. Shen, Y. Xiao, and H.R. Du. Impurity effects on ion temperature gradient driven multiple modes in transport barriers. *Nuclear Fusion*, 59(7):076013, may 2019.

[15] J. Li, Z.X. Wang, J.Q. Dong, Y. Shen, L.F. Wang, M.K. Han, and H.R. Du. Quasi-linear heat transport induced by ITG turbulence in the presence of impurities. *Nuclear Fusion*, 60(12):126038, oct 2020.

[16] J. Li, Z.X. Wang, J.Q. Dong, Y. Shen, X.L. Zou, W.L. Zhong, H.R. Du, L.F. Wang, M.K. Han, X.R. Zhang, J.Y. Liu, G.L. Xiao, and A.S. Liang. Impurity effects on quasi-linear heat transport induced by interaction of TEM and ITG turbulence. *Nuclear Fusion*, 61(12):126008, oct 2021.

[17] H.R. Du, Z.X. Wang, J.Q. Dong, and S.F. Liu. Coupling of ion temperature gradient and trapped electron modes in the presence of impurities in tokamak plasmas. *Physics of Plasmas*, 21(5):052101, 05 2014.

[18] H.R. Du, Z.X. Wang, and J.Q. Dong. Impurity effects on short wavelength ion temperature gradient mode in elongated tokamak plasmas. *Physics of Plasmas*, 22(2):022506, 02 2015.

[19] H.Q. Wang, G.S. Xu, B.N. Wan, S.Y. Ding, H.Y. Guo, L.M. Shao, S.C. Liu, X.Q. Xu, E. Wang, N. Yan, V. Naulin, A.H. Nielsen, J. Juul Rasmussen, J. Candy, R. Bravenec, Y.W. Sun, T.H. Shi, Y.F. Liang, R. Chen, W. Zhang, L. Wang, L. Chen, N. Zhao, Y.L. Li, Y.L. Liu, G.H. Hu, and X.Z. Gong. New Edge Coherent Mode Providing Continuous Transport in Long-Pulse H-mode Plasmas. *Physical Review Letters*, 112:185004, May 2014.

[20] Y. Ye, G.S. Xu, B.N. Wan, R. Chen, N. Yan, H.Y. Guo, L.M. Shao, Q.Q. Yang, H.Q. Wang, W. Zhang, T.Y. Xia, T. Zhang, Y.Y. Li, T.F. Wang, Q. Zang, Y.J. Hu, G.J. Wu, L. Zhang, B.L. Hao, L. Wang, Y.L. Li, X.Q. Wu, L. Chen, H. Lan, Y.F. Wang, J.C. Xu, G.H. Hu, S.Y. Ding, H. Zhang, N. Zhao, J. Li, and The EAST Team. A stationary long-pulse ELM-absent H-mode regime in EAST. *Nuclear Fusion*, 57(8):086041, jul 2017.

[21] Y. Ye, R. Chen, G.S. Xu, L. Wang, H.Y. Guo, C. Zhou, Y.F. Wang, J.C. Xu, X. Lin, Y.M. Wang, Q. Zang, Y.M. Duan, L. Zhang, J.B. Liu, X.Q. Wu, Q.Q. Yang, G.S. Li, and B.N. Wan. Study

on pedestal fluctuations in H-modes without large ELMs during the transition to a detached tungsten divertor in EAST. *Nuclear Fusion*, 61(12):126050, nov 2021.

[22] C. Zhao, T. Zhang, and Y. Xiao. Gyrokinetic simulation of dissipative trapped electron mode in tokamak edge. *Physics of Plasmas*, 24(5):052509, 05 2017.

[23] B.Y. Xie, L. Ye, Y. Chen, P.F. Zhao, Y. Ye, X. Lin, H. Lan, W.F. Guo, and N. Xiang. Global gyrokinetic simulation of edge coherent mode in EAST. *Nuclear Fusion*, 63(2):026017, jan 2023.

[24] X. X. Zhang, H. S. Cai, and Z. X. Wang. Influence of deeply trapped energetic ions on tearing modes. *Physics of Plasmas*, 26(6):062505, 06 2019.

[25] P.J. Catto and K.T. Tsang. Trapped electron instability in tokamaks: Analytic solution of the two-dimensional eigenvalue problem. *Physics of Fluids*, 21(8):1381–1388, 08 1978.

[26] S.C. Guo and F. Romanelli. The linear threshold of the ion-temperature-gradient-driven mode. *Physics of Fluids B: Plasma Physics*, 5(2):520–533, 02 1993.

[27] J.W. Connor, R.J. Hastie, and P. Helander. Stability of the trapped electron mode in steep density and temperature gradients. *Plasma Physics and Controlled Fusion*, 48(6):885, may 2006.

[28] H.S. Xie, Y.Y. Li, Z.X. Lu, W.K. Ou, and B. Li. Comparisons and applications of four independent numerical approaches for linear gyrokinetic drift modes. *Physics of Plasmas*, 24(7):072106, 06 2017.

[29] J.C. Adam, W.M. Tang, and P.H. Rutherford. Destabilization of the trapped-electron mode by magnetic curvature drift resonances. *The Physics of Fluids*, 19(4):561–566, 04 1976.

[30] H. T. Chen and L. Chen. On drift wave instabilities excited by strong plasma gradients in toroidal plasmas. *Physics of Plasmas*, 25(1):014502, 01 2018.

[31] Pueschel£¬M. J., D. R. Hatch, D. R. Ernst, W Guttenfelder, P. W. Terry, J. Citrin, and J. W. Connor. On microinstabilities and turbulence in steep-gradient regions of fusion devices. *Plasma Physics and Controlled Fusion*, 61(3):034002, feb 2019.

[32] I. Sandberg, H. Isliker, and V.P. Pavlenko. Finite Larmor radius effects on the coupled trapped electron and ion temperature gradient modes. *Physics of Plasmas*, 14(9):092504, 09 2007.

[33] T. Fülöp, I. Pusztai, and P. Helander. Collisionality dependence of the quasilinear particle flux due to microinstabilities. *Physics of Plasmas*, 15(7):072308, 07 2008.

[34] Y. Q. Tao, G. S. Xu, K. Wu, Q. Q. Yang, L. Wang, Q. P. Yuan, Y. F. Wang, X. Lin, L. Y. Meng, G. F. Ding, L. Yu, R. Chen, J. B. Liu, N. Yan, H. Lan, P. J. Sun, K. D. Li, J. C. Xu, Y. M. Duan, Q. Zang, Y. F. Jin, L. Zhang, S. X. Wang, K. N. Geng, and R. R. Liang. Long-pulse H-mode operation with stored-energy monitoring for detachment feedback control with a new lower tungsten divertor in EAST. *Nuclear Fusion*, 63(7):076008, may 2023.

[35] X. D. Yang, X. Z. Gong, J. P. Qian, Y. F. Jin, P. Manas, P. Li, C. Bourdelle, Y. Q. Chu, B. Zhang, Y. J. Chen, Y. C. Hu, Y. Y. Li, K. D. Li, X. X. Zhang, Y. M. Duan, H. M. Zhang, T. Q. Jia, H. Q. Liu, Q. Zang, J. Huang, R. Ding, L. Wang, and G. S. Xu. Mechanism of enhanced ion temperature by impurity seeding in east h-mode plasma. *Nuclear Fusion*, 64(1):016030, dec 2023.

[36] G. Q. Xue, W. L. Zhong, X. L. Zou, G. L. Xiao, A. S. Liang, L. Liu, X. X. He, D. L. Yu, M. Jiang, Z. C. Yang, K. R. Fang, Z. B. Shi, J. M. Gao, J. Li, M. K. Han, J. Q. Dong, Z. X. Wang, C. Y. Chen, J. Yin, B. B. Feng, K. Zhang, C. F. Dong, C. H. Liu, J. Wen, P. W. Shi, Y. P. Zhang, N. Wu, T. B. Wang, Y. Liu, M. Xu, and X. R. Duan. Enhancement of plasma ion temperature by impurity seeding in h-mode plasmas. *Nuclear Fusion*, 61(11):116048, oct 2021.

[37] N. Bonanomi, P. Mantica, J. Citrin, C. Giroud, E. Lerche, C. Sozzi, D. Taylor, M. Tsalas, D. Van Eester, and JET contributors. Effects of nitrogen seeding on core ion thermal transport in JET ILW L-mode plasmas. *Nuclear Fusion*, 58(2):026028, jan 2018.

[38] G. Tardini, R. Fischer, F. Jenko, A. Kallenbach, R. M. McDermott, T. Pöutterich, S. K. Rathgeber, M. Schneller, J. Schweinzer, A. C. C. Sips, D. Told, E. Wolfrum, and the ASDEX Upgrade Team. Core transport analysis of nitrogen seeded H-mode discharges in the ASDEX Upgrade. *Plasma Physics and Controlled Fusion*, 55(1):015010, dec 2012.

[39] P.J. Sun, Y.D. Li, Y. Ren, X.D. Zhang, G.J. Wu, Y.M. Wang, Y. Liu, T.F. Zhou, X. Gu, X.Q.

Yuan, Q. Zang, P. Li, Y.J. Chen, Y.M. Duan, S.T. Mao, B. Zhang, T.H. Shi, H.Q. Liu, B. Lyu, L.Q. Hu, and J.G. Li. Experimental study of high-k turbulence during an energy confinement degradation phase in east ohmic plasmas. *Nuclear Fusion*, 60(4):046016, feb 2020.